In Situ Oxidation Studies of High-Entropy Alloy Nanoparticles

Boao Song[1], Yong Yang[2,3], Muztoba Rabbani[4], Timothy T. Yang[4], Kun He[5], Xiaobing Hu[5], Yifei Yuan[1], Pankaj Ghildiyal[3], Vinayak P. Dravid[5], Michael R. Zachariah[3], Wissam A. Saidi[4*], Yuzi Liu[6*], Reza Shahbazian-Yassar[1*]*

[1.] *Department of Mechanical and Industrial Engineering, University of Illinois at Chicago, Chicago, Illinois 60607, United States.*

[2] *Department of Chemical and Biomolecular Engineering, University of Maryland College Park, Maryland 20742, United States.*

[3.] *Department of Chemical Engineering and Materials Science, University of California Riverside, Riverside, California 92521, United States.*

[4.] *Department of Mechanical Engineering and Materials Science, University of Pittsburgh, Pittsburgh, Pennsylvania 15261, United States.*

[5.] *Department of Materials Science and Engineering, International Institute for Nanotechnology (IIN), Northwestern University Atomic and Nanoscale Characterization Experimental (NUANCE) Center, Northwestern University, Evanston, Illinois 60208, United States.*

[6.] *Center for Nanoscale Materials, Argonne National Laboratory, Argonne, Illinois 60439, United States.*

** Correspondence to: rsyassar@uic.edu; yuziliu@anl.gov; alsaidi@pitt.edu; mrz@engr.ucr.edu*

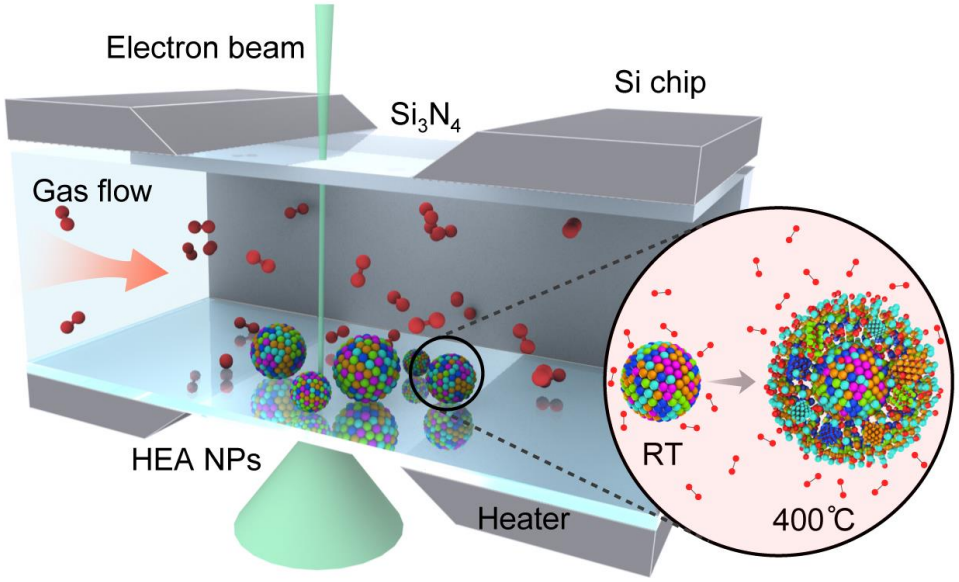

TOC Graphic. *In situ* (S)TEM device to study HEA NPs oxidation in atmospheric pressure air environment.

Abstract

Although high-entropy alloys (HEAs) have shown tremendous potentials for elevated temperature, anti-corrosion, and catalysis applications, little is known on how HEA materials behave under complex service environments. Herein, we studied the high-temperature oxidation behavior of $Fe_{0.28}Co_{0.21}Ni_{0.20}Cu_{0.08}Pt_{0.23}$ HEA nanoparticles (NPs) in atmospheric pressure dry air environment by *in situ* gas-cell transmission electron microscopy (TEM). It is found that the oxidation of HEA NPs is governed by Kirkendall effects with logarithmic oxidation rates rather than parabolic as predicted by Wagner's theory. Further, the HEA NPs are found to oxidize at a significantly slower rate compared to monometallic NPs. The outward diffusion of transition metals and formation of disordered oxide layer is observed in real time and confirmed through analytical energy dispersive spectroscopy (EDS) and electron energy loss spectroscopy (EELS) characterizations. Localized ordered lattices are identified in the oxide suggesting the formation of Fe_2O_3, CoO, NiO and CuO crystallites in an overall disordered matrix. Hybrid Monte Carlo (MC) and molecular dynamics (MD) simulations based on first-principles energies and forces support these findings, and show that the oxidation drives surface segregation of Fe, Co, Ni, and Cu while Pt stays in the core region. The present work offers key insight into how HEA NPs behave under high-temperature oxidizing environments, and shed light on future design of highly stable alloys with wide application possibilities.

Keywords: high-entropy alloys, nanoparticles, *in situ* TEM, oxidation, phase segregation, Kirkendall

High-entropy alloys, an emerging alloy compound involving five or more principle elements in the form of homogeneous mixed disordered solid solutions, is attracting increased attention because of their superior properties compared to conventional alloys including high mechanical strength, high thermal stability, and better corrosion resistance.[1-4] The successful fabrication of such HEAs has emerged rapidly over the last two decades involving bulk melting,[5,6] solid-state processing,[7-9] physical vapor deposition,[10] and additive manufacturing.[11-13] Notably, the lately developed carbothermal shock method[14] allows incorporating multiple metal elements into single-phase HEA NPs and thus provides wide possible applications in catalysis, electronics, structural alloys, and so forth. Further, the recently developed scalable aerosol synthesis[15] method takes a further step towards production of HEA NPs in bulk manufacturing quantities with full potential for industrial applications.

Similar to conventional alloys, industrial service environments for HEAs usually involve critical conditions such as exposure to high-temperature and oxidizing/reducing gases, acidic and chloride-containing solutions.[16] Several studies have been devoted to understand the corrosion behaviors of HEAs such as oxidation in air[17-21]and oxygen-containing atmospheres.[22] Although most HEAs show single-stage parabolic oxidation kinetics such as FeCoNiCr-based quinary systems at 700-900 °C,[18] AlCoCrCuFeNi at 800 °C,[17] and $Al_x(NiCoCrFe)_{1-x}$ at 1050 °C,[19] two-stage linear and parabolic kinetics can be observed for FeCoNiCrMn HEA below 900 °C.[20, 22] Composition-dependent multiple oxidation scales were formed in HEA oxides in either layer-to-layer[17,18,22] or precipitation[19] mechanisms. However, these studies are focused on bulk HEAs and there is still very limited knowledge of how HEA NPs behave under such environments. One of the key challenges for such nanometer-size HEA NPs is in obtaining structural and

compositional information at high spatial and temporal resolution, which requires advanced characterization techniques including TEM. Recently, the development of *in situ* open-cell[23-27] and closed-cell[28-33] environmental TEM with capability of exposing sample to atmospheric pressure gas environments provides the possibility to study materials behavior under realistic application conditions in real-time. Previous studies have shown that the materials' behavior under redox reactions can be captured including facet evolution of Pt NPs[33] and PdCu,[30] phase segregation in bimetallic Pt-Ni[32] and PdCu NPs,[28] sintering of Co,[31] Pt and core-shell NPs.[34] Benefiting from the *in situ* gas-cell TEM, we studied the high-temperature oxidation behavior of $Fe_{0.28}Co_{0.21}Ni_{0.20}Cu_{0.08}Pt_{0.23}$ HEA NPs in atmospheric pressure air environment. The structural and compositional evolution during oxidation at 400 °C are captured in real-time through (scanning) transmission electron microscopy (S)TEM imaging and EDS/EELS analyses. It is found that the HEA NPs' oxidation kinetics are governed by logarithmic rate constants and are guided by Kirkendall effect involving outward diffusion of transition metals including Fe, Co, Ni and Cu. Anisotropic oxidation is observed on adjacent HEA NPs such that oxide prefers to initiate at their connecting interface. The oxide layer is found to have a disordered mixture of Fe_2O_3, CoO, NiO and CuO crystallites in their Fe^{3+}, Co^{2+}, Ni^{2+} and Cu^{2+} oxidation states. Hybrid MC/MD simulations based on first-principles calculations support these findings and show that under oxidizing conditions there is a preferential surface segregation of Fe, Co, Ni, and Cu while Pt remains in the core of the NP.

Results and discussion

In the first step, the atomic ordering and chemical composition of the as-synthesized HEA NPs were studied. The NPs were prepared *via* aerosol synthesis method as reported in our earlier work.[15] The

morphology and chemical composition of synthesized HEA NPs were characterized by STEM, EDS and EELS. High-angle annular dark-field (HAADF) image in Figure 1a shows that the HEA NPs are mostly spherical with particle size ranging from 50 to 200 nm. Figure 1b is a low-angle annular dark-field (LAADF) image focused on an individual NP with facetted edges. The boxed region was selected for atomic resolution HAADF and annular bright-field (ABF) imaging as shown in Figure 1c. The lattice distortion and random atom-to-atom contrast variation suggests a homogeneous mixing of Fe, Co, Ni, Cu and Pt at the atomic level. Inset in the ABF image shows the fast Fourier transform (FFT) patterns in <100> zone axis with $(00\bar{2})$ and (022) planes highlighted, confirming the successfully synthesized single-phase HEA NPs with face-centered cubic (FCC) crystal structure, which is consistent with our previous reported X-ray powder diffraction (XRD) results.[15] The composition uniformity was confirmed by both STEM-EELS and STEM-EDS mappings. STEM-EELS mapping was performed on a NP in <110> zone axis as shown in Figure 1d. The crystal contains regions with appreciable twining as suggested in FFT and marked by dashed lines. The EELS mappings in red shadowed region from Fe, Co, Ni, Cu *L*-edges and Pt *M*-edge are shown in Figure 1e. In all cases, Fe, Co, Ni, Cu and Pt are found to be distributed homogeneously. In addition, elemental distribution from STEM-EDS mapping in the sample region of Figure 1a is shown in Figure 1f. These further confirm that all the synthesized NPs, irrespective of their sizes, have well-mixed elemental compositions. The composition of each HEA NP is obtained from EDS analysis (Supporting Information Figure S1) and the averaged HEA composition is determined to be $Fe_{0.28}Co_{0.21}Ni_{0.20}Cu_{0.08}Pt_{0.23}$.

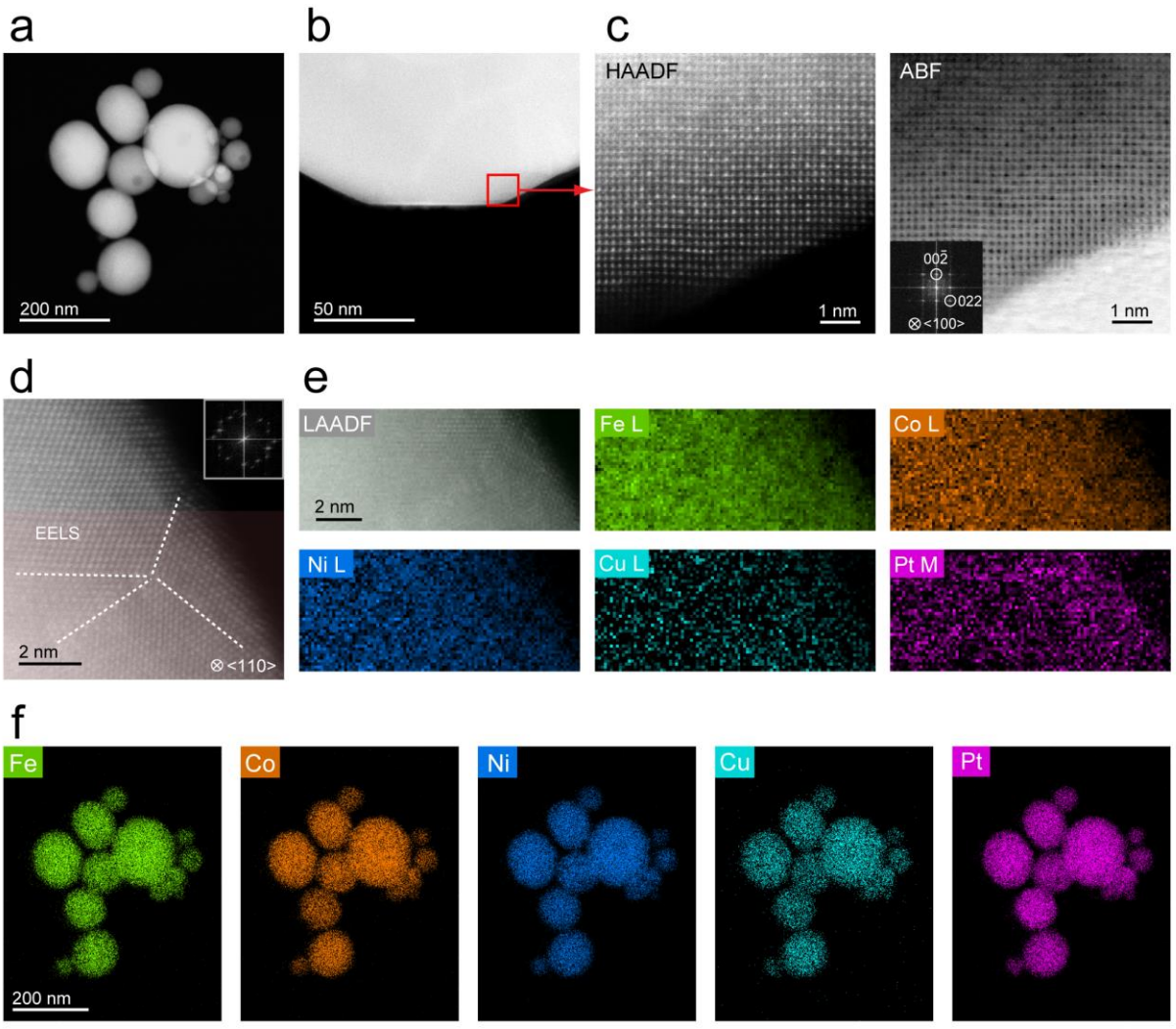

Figure 1. Atomic structure and chemical characterization of HEA NPs. (**a**) HAADF image showing the as-synthesized HEA NPs. (**b**) LAADF image focusing on the edge of an individual HEA NP. (**c**) HAADF and ABF images from the boxed region in **b**, showing the atomic structure of HEA in <100> zone axis. The inset in ABF image is the corresponding FFT with highlighted diffraction spots from (00$\bar{2}$) and (022) planes. (**d**) LAADF image of HEA in <110> zone axis with twining marked with dashed lines. The inset shows the corresponding FFT with multiple diffraction spots from twining. Red shadowed region marks the EELS mappings area. (**e**) EELS mappings from region in **d**. Signals are extracted from *L*-edges of Fe, Co, Ni, Cu and *M*-edge of Pt. (**f**) EDS mappings of the HEA NPs in **a**.

Figure 2a shows a schematic illustration of the specimen holder employed for the *in situ* gas-cell TEM experiments. Atmospheric pressure can be maintained inside the cell with continuous gas flow benefiting from the isolated environment formed by a pair of microchips.[29, 34-36] The *in situ* experiment was performed in air environment as shown in Movie S1. The beginning of the movie is exactly at the same time of starting the heating process. Snapshots from Movie S1 are shown in Figure 2b. The HEA NPs underwent oxidation in atmospheric air and an oxide layer can be seen to grow gradually covering the NPs, shown as the lighter contrast layer on HEA NPs. To present this more visibly, the zoomed-in images of the boxed regions in the first frame are shown in Figure 2c and d, with purple box corresponding to one small NP (less than 100 nm) and blue box focusing on top surface of the larger NP ~ 130 nm. The small NP has a thin oxide layer all around the nanoparticle, while the oxide layer on large NPs are thick and not uniform that becomes noticeable starting from ~13.3 min. Compared to our *in situ* oxidation of monometallic Co NPs in similar size at 400 °C (Movie S2), it is clear that Co transferred from solid NPs to hollow structures in less than one minute. Moreover, bimetallic alloy NPs were also observed to show full oxidation in less than 30 mins forming porous and hollow structures such as NiFe NPs in air[23] and NiCr NPs in low pressure (1 mbar) O_2,[26] as well as the formation of obvious voids for NiCo NPs accompanied by the outward diffusion of Ni and Co.[37] For HEA NPs presented here, formation of voids and hollow structures in similar size range are not observed, suggesting that the overall oxidation kinetics are slower than both mono and bimetallic alloy NPs with similar principle elements. The oxide layer thickness d_{OX} was plotted in Figure 2e after measurement following the same direction as indicated in the arrows in Figure 2c and d. For the small NP, oxidation kinetics can be perfectly fitted with a logarithmic law $d_{OX} = K \ln(t - A)$ with oxidation rate K determined to be 1.72. The oxidation kinetics

follow logarithmic law rather than parabolic predicted by Wagner theory,[38] suggesting that the growth of oxide layer is governed by combined effects involving electric field and lattice diffusion. The reason can be that Wagner's theory assumes a planar geometry, while for HEA NPs considering the spherical geometry with surface curvature, the oxidation kinetics can be altered by surface charge and space charge distribution. Since there is much stronger polarization in spherical NP than planar surface,[39] the electric field[40] across the oxide in radial direction[41] will result in a faster growth rate compared to parabolic relationship in the initial stage and slower rate in longer time range that fits into the logarithmic law. As seen in Figure 2e, the larger NP, again follows logarithmic law with K_1 equal to 1.46 in the first 10.7 min but has a burst of oxide growth starting at ~13.3 min. The oxidation kinetics afterwards can also be fitted with a logarithmic function with $K_2 = 6.87$, indicating a much faster oxidation rate. This anomalous two-stage oxidation kinetics seems to happen selectively at the region where two HEA NPs are adjacent (highlighted by blue arrows in Figure 2b), while the surface without adjacent NPs displays only one-stage oxidation kinetics (purple arrows in Figure 2b). Existing high-temperature oxidation models[42] (Valensi-Carter and Fromhold) taking spherical geometry into consideration predict that smaller NPs can be oxidized faster than larger NPs, which is consistent with our experimental observation within first ~10.7 min. The much increased oxidation rate after 13.3 min for large NP in its second oxidation stage may be attributed to the sintering induced atomic surface diffusive flux close to the interfaces where HEA NPs are in contact,[43] resulting in a change of electric-field induced concentration gradient in initial oxide and provide extra driving force for metal outward diffusion.[43-45] In addition, the oxidation kinetics of HEA NPs are compared with monometallic Co NPs as plotted in Figure S2. The 55 nm Co NP oxide thickness increases to 25 nm in less than 1.2 minute of oxidation, however there is no visible oxidation in HEA NPs

at the same time frame. This confirms the much slower oxidation behavior in HEA NPs. The clear mechanisms are yet to be determined while more systematic analysis on HEA NPs' properties are necessary taking into account parameters such as built-in pressure,[44] strain,[46,47] and electric field[41] in such HEA NP systems.

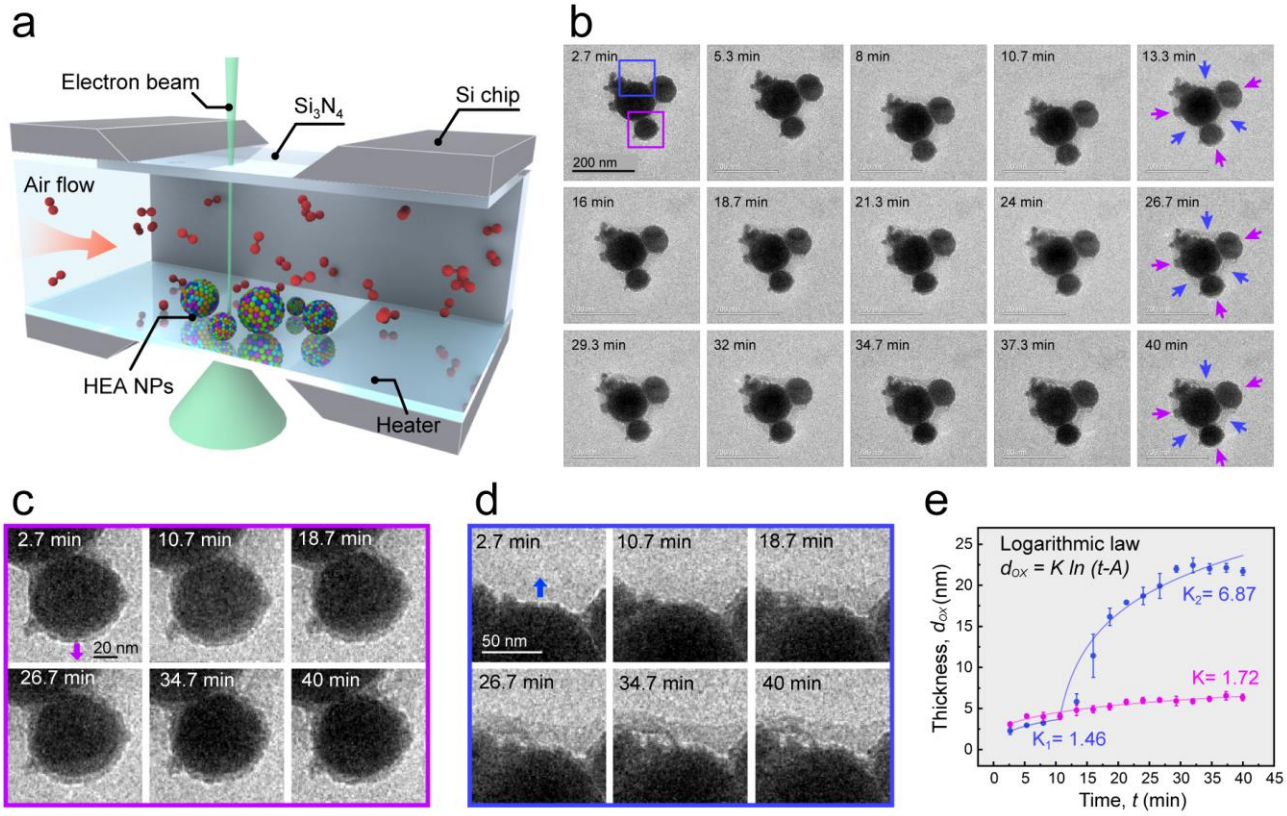

Figure 2. Oxidation of HEA NPs in air. (**a**) Schematic of the *in situ* gas-cell (S)TEM device to study the oxidation of HEA NPs. (**b**) *In situ* TEM image sequences of HEA NPs during annealing in air. (**c, d**) TEM image sequences focused on the two boxed regions in **b** during annealing in air. (**e**) Oxide thickness as a function of time measured from the direction highlighted in **c** and **d**.

To gain understanding on the chemical composition after oxidation, the HEA NPs were characterized by STEM-EDS and STEM-EELS as shown in Figure 3. HAADF and LAADF images in Figure 3a show

the same HEA NP region after *in situ* oxidation. Apparently, the LAADF image show more clearly the oxide region with a brighter contrast due to the higher signal-to-noise ratio (SNR) in scattering at low angles for oxygen-containing compounds. In the STEM-EDS maps, transition metals of Fe, Co, Ni and Cu are all seen to present in the oxide layer, while Pt is the only metal that does not segregate to the surface. Combining with selected overlaid maps (Figure S3) it is clear that 1) in the region without oxygen, HEA NPs still show a homogeneous mixing of Fe, Co, Ni, Cu and Pt; 2) Fe, Co, Ni and Cu can be found in the region with oxygen; and 3) Cu is the most widely dispersed in the oxide region. Further, quantitative EDS analysis were extracted from the maps in the two boxed regions focusing on the large NP and are shown in Figure 3b and S3b. The boxed regions were aligned with the plots with corresponding colors. The NP surface is defined as the boundary of the brightest contrast in LAADF images (marked by dashed lines) so the outward direction indicates oxide region. The two plots show same trends where Fe, Co, Ni and Cu show outward diffusion while Pt does not display outward segregation and is not present in the oxide layer. Among the transition metals, Co is more accumulated in the oxide region closer to HEA surface within ~20 nm, and Cu is more presented in the region farther away; Fe and Ni are distributed in a more monotonic decreasing manner in the oxide. These results show the oxidation of HEA NPs is guided by Kirkendall effects, where metals diffuse outward at different rates to react with oxygen. This leads to a composition variation in the oxide layer and HEA core. Further, to exclude the influence of electron beam during *in situ* observation, STEM-EDS on HEA NPs on other regions without the electron beam exposure are shown in Figure S4 and discussed in Supporting Note S1. The results show that 1) there is no significant difference in composition and 2) more Kirkendalls voids are seen in the larger HEA NPs.

The STEM-EELS analyses on *ex situ* oxidized HEA NPs are shown in Figure 3c-g (first method, details in Method section). ADF image in Figure 3c shows the oxide layer on HEA NPs after oxidation, and the EELS mappings (Figure 3d) from small red boxed region again confirm that the oxide layer contains Fe, Co, Ni and Cu. The EEL spectra from the mapping region is then extracted following the direction of the rainbow arrow and are plotted in Figure 3e. Although subtle changes of transition metal $L_{2,3}$-edges are hard to discern in the current energy resolution, there are obvious variations on O *K*-edge especially the pre-peak intensity and energy separation between pre-peak and main peak when it is closer to NP surface, as highlighted by red arrows. Further, with a larger EELS mapping area (larger boxed region in Figure 3c) covering the whole HEA NP, multiple linear least squares (MLLS) fitting results is shown in Figure 3f. The fitting is performed using *L*-edges reference spectra of as-synthesized HEA, Fe_2O_3, CoO, NiO and CuO,[48-53] and is shown in the same sequence. The last image is a directly extracted O-*K* map for the ease of comparison. These MLLS fitting results serve as valence state maps of Fe, Co, Ni and Cu. It can be seen that Fe^{3+}, Co^{2+}, Ni^{2+}, and Cu^{2+} are all present in the oxide layer region, suggesting that in the oxide Fe is in 3+ state while Co, Ni and Cu are in 2+ state. This is consistent with a previous study[54] showing that among various stoichiometry of oxides, Fe_2O_3 and CuO are more favorable in high oxygen concentrations. Figure 3g shows energy loss near edge fine structure (ELNES) of L_3/L_2 white-line intensity ratio for Fe and Co and O-K on another similar size HEA NP. It is known that the transition metal L_3/L_2 white-line ratio is directly correlated with *3d* orbital occupancy that a higher ratio indicates increased oxidation state for Fe[55] while a lower ratio indicates higher oxidation state[56,57] for Co. Here, Fe L_3/L_2 white-line ratio displays an increase in the external oxide (positive distance to surface) region suggesting a more oxidized Fe state compared to the interior of HEA NP. Likewise, Co L_3/L_2 white-line

ratio gradually decreases from NP interior to surface and drop further in external oxide region, suggesting an upward gradient of Co oxidation state. The third plot in Figure 3g shows distance of O *K*-edge pre-peak to main peak (energy separation, ΔE) as a function of distance to HEA surface. Although the ELNES of O *K*-edge contains metal-oxygen bonding information contributed by four transition metals involving Fe, Co, Ni and Cu, an increase of ΔE from interior to surface can still be identified indicating the higher overall oxidation states in the oxide region.[58]

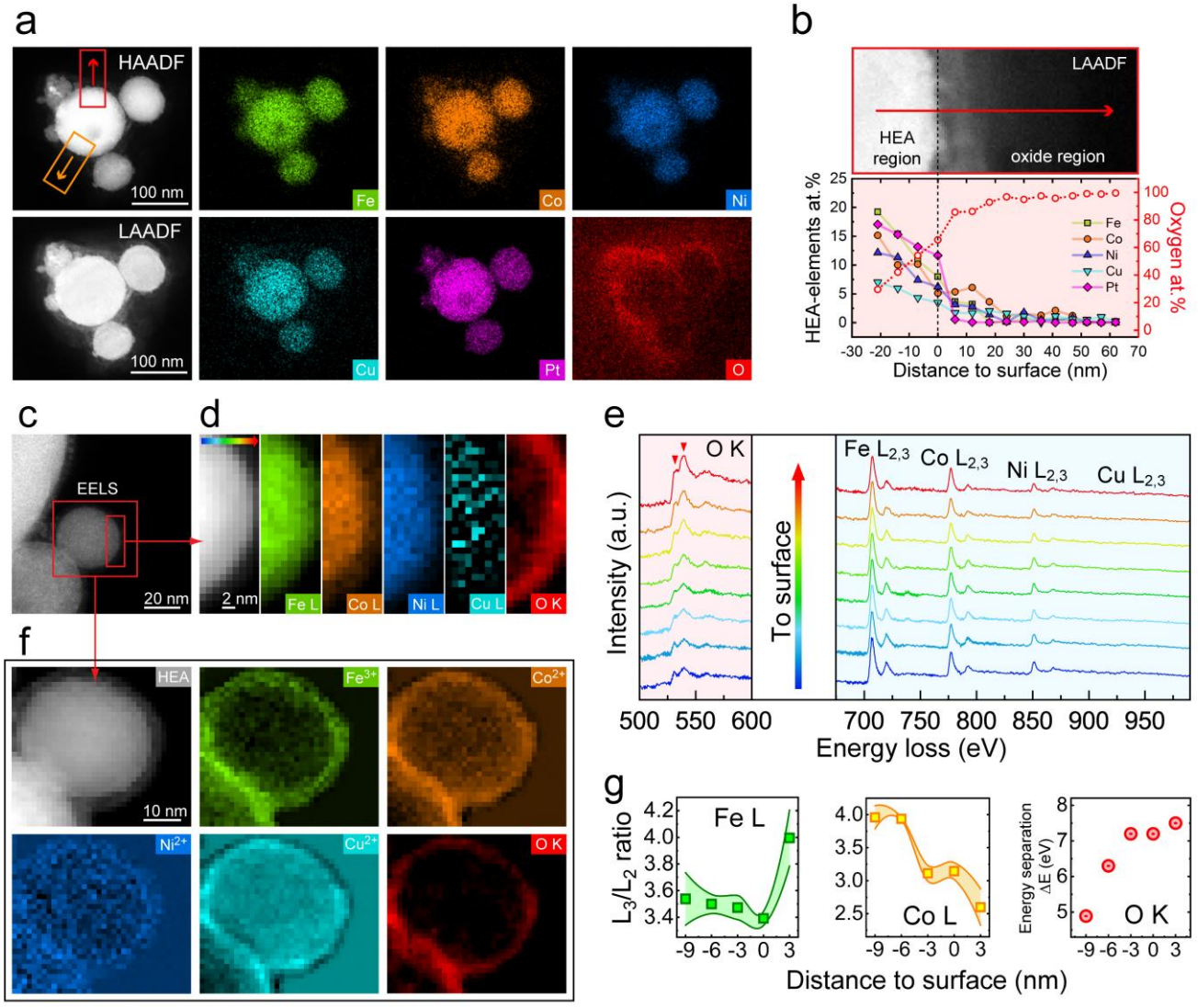

Figure 3. Chemical analysis of HEA NPs after oxidation in air. (**a**) *Post situ* HAADF and LAADF images of the same HEA NPs after *in situ* oxidation in Figure 2, followed by EDS mappings of Fe, Co, Ni, Cu, Pt

and O. (**b**) LAADF images from red boxed regions in **a** and corresponding at. % distribution of Fe, Co, Ni, Cu, Pt and O extracted from EDS maps. The arrows in LAADF images indicate the same directions as the arrows in **a**. The zero in the horizontal axis (distance to surface) represent the edge of NP marked by dash lines, while positive values stand for outward directions. (**c**) ADF image showing HEA NPs after *ex situ* oxidation in air. (**d**) Spectrum image corresponding to smaller red boxed region in **c** and EELS maps extracted from Fe, Co, Ni, Cu $L_{2,3}$-edges and O *K*-edge. (**e**) EEL spectra extracted from the spectrum image in **d** in the direction marked by rainbow arrow. The O pre-peak and main peak maximum marked with red arrows are highlighted with dash lines. (**f**) EELS MLLS fitting showing the valence state map from larger red boxed region in **c**. The maps are displayed in sequence of fitting results from reference spectra of as-synthesized HEA, Fe_2O_3, CoO, NiO and CuO. The last map was extract directly from O *K*-edge. (**g**) Fe and Co L_3/L_2 white-line intensity ratio as function of distance to surface obtained from another HEA NP after oxidation. Zero in horizontal axis represent the edge of NP, while positive values stand for outward directions. The third plot shows energy difference between O *K*-edge pre-peak and main peak (energy separation, ΔE) as function of distance to HEA surface.

Next, high-resolution TEM (HRTEM) images were successfully obtained on HEA NPs discussed in Figure 2 after oxidation. The first row in Figure 4a-c show exemplar HRTEM images with HEA and oxide region highlighted. The corresponding FFTs are shown in the second row, with diffraction spots marked with *d*-spacings. Since the largest *d*-spacing in FCC HEA NPs is 0.214 nm from {111} planes, any observed *d*-spacing larger than that should originate from the oxides. As such, in FFTs the diffraction spots are labeled as the most possible crystal planes from HEA or oxide compounds. Examples are shown

as $\{111\}_{CoO}$ in Figure 4a, $\{111\}_{NiO}$ in Figure 4b, $\{110\}_{Fe2O3}$ or $\{002\}_{CuO}$, $\{006\}_{Fe2O3}$ or $\{200\}_{CoO}$ in Figure 4c. To clearly validate the oxides, inverse FFTs (IFFTs) were shown in both Figure 4a-c by masking each pair of diffraction spots. As seen, starting from third row in Figure 4a, for instance, $\{111\}_{HEA}$ are only from HEA region, while $\{111\}_{CoO}$ are mostly in the oxide layer. Following the same trend, Figure 4b and c show that crystal planes from oxide compounds are only presented in oxidized regions. After carefully analyzing all the HRTEMs, the lattice *d*-spacings not likely to belong to HEA are plotted as dashed signs in Figure 4d. The *d*-spacings from planes in HEA and some oxide compounds are shown for reference. The first and second columns named HEA_T and HEA_X are based on (S)TEM and XRD analysis, respectively. Those *d*-spacings not belonging to HEA are likely to originate from oxides including Fe_2O_3, CoO, NiO, and CuO. The results show consistency with previous valence state analyses on *ex situ* oxidized HEA NPs where Fe^{3+}, Co^{2+}, Ni^{2+}, and Cu^{2+} are identified. There are also possibilities that these ordered lattices originate from complex oxides involving more than one metal elements, however it is not possible to properly index them due to the lack of standard lattice parameters. The results further suggest that although the oxide lattices are not observed to be homogeneous in all oxide regions, there is ordered oxide crystallites in the disordered oxide matrix containing Fe, Co, Ni, Cu and O. While principle elements including Fe, Co, Ni and Cu typically form crystalline oxide under similar oxidation conditions, the observed disordered oxide with only localized oxide crystallites can be ascribed to sluggish diffusion and factors that lower the total Gibbs free energy of disordered oxide compared to crystalline oxide: 1) atoms are expected to be trapped in their local positions if diffusion is sluggish and may form only short range ordering that may not go beyond a few nanometers, 2) built-in high entropy in the HEA NPs that lower the positive contribution of interfacial energy between HEA and disordered oxide interface,[59] and 3) the

strain-induced by the lattice mismatch between an epitaxial HEA and crystalline metal oxide interface at curvature regions that increase the interfacial energy contribution.[32] Therefore, compared to single element NPs, our atomistic studies show that HEA NPs can form disordered oxides. Considering the disordered oxide can serve as a diffusion barrier[60] and the possible sluggish diffusion in HEA, they can be the reason that HEA NPs display slower oxidation kinetics compared to monometallic or bimetallic NPs.

The structural information is also studied on *ex situ* oxidized HEA NPs (first method in Method section). For ABF image in Figure 4e, the oxide layer can be seen in the lower contrast region close to the HEA surface. A significant number of voids of less than 10 nm in size are clearly observed and exemplar of them marked by red arrows. Larger voids are expected to form after these tiny ones accumulate and coalesce. Figure 4f shows a pair of HAADF and ABF images of HEA NP in <110> zone axis. FFT (inset in ABF image) indicates an FCC pattern of HEA NP. While no lattice can be resolved in the oxide layer region, clearly the HEA NP maintains its FCC structure as evident through the same atomic arrangement in comparison to as-synthesized sample (Figure 1d). This is true even at the void regions (marked by red arrows) suggesting that the atomic outward diffusion during oxidation does not break the FCC crystal structure. This is consistent with HRTEM in Figure 4a that $\{111\}_{HEA}$ can be resolved. Pair of HAADF and ABF images in Figure 4g show another HEA NP in <110> zone axis with identifiable twining (marked by dashed lines). Although it is not clear whether the twining existed initially or formed after oxidation, the FCC structure in HEA NP is confirmed to remain unchanged. This is also consistent with the second *ex situ* oxidation results (details in Method section) discussed in Supporting Note S2 and Figure S5.

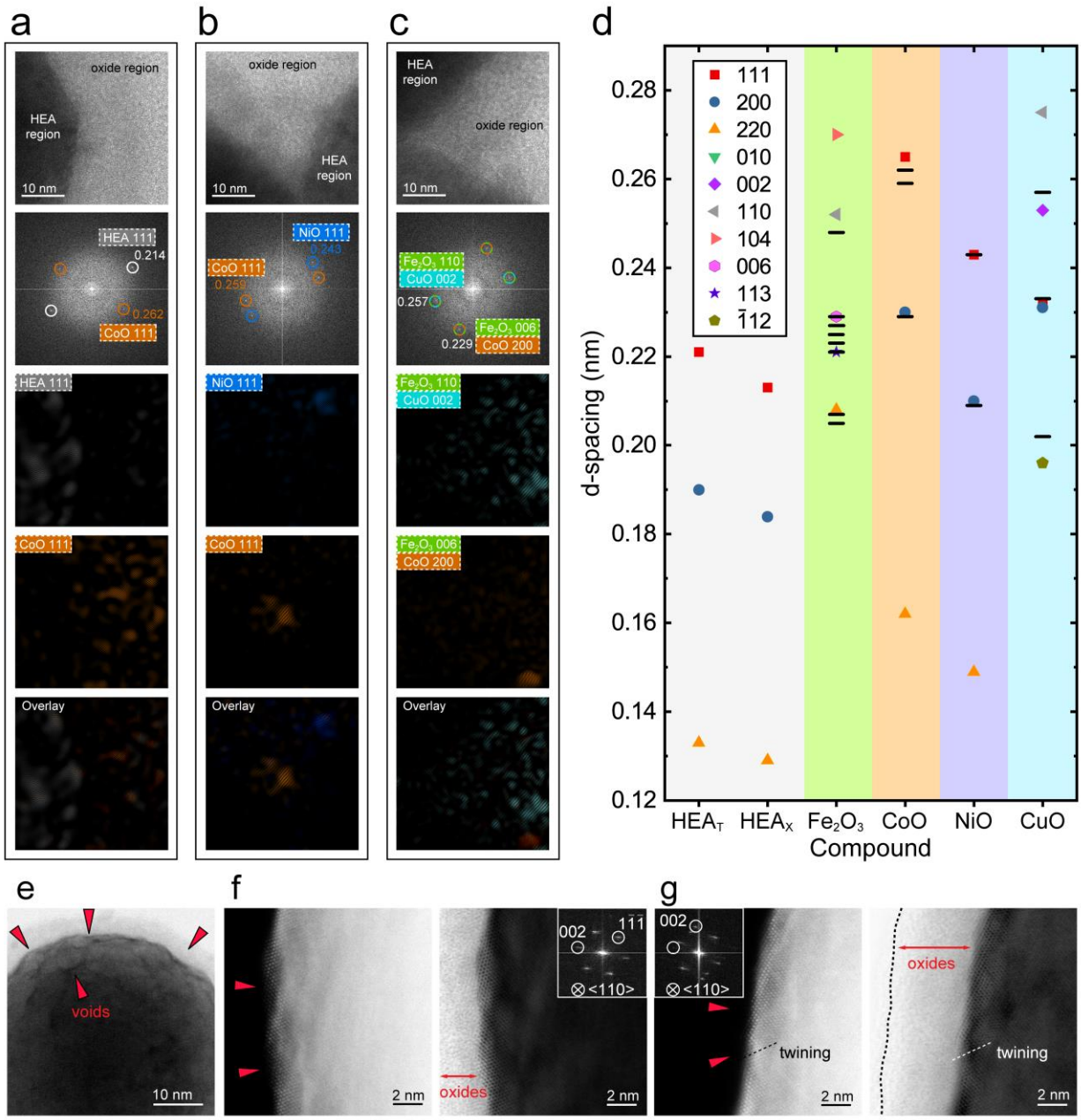

Figure 4. HRTEM analysis of HEA NPs after oxidation in air. (**a-c**) Three exemplar HRTEM images and the corresponding FFTs of HEA NPs after *in situ* oxidation in air. In the FFTs, diffraction spots are highlighted according to the most possible crystal planes in HEA or oxide phases. The last three rows show the IFFT of masked diffraction spots with corresponding phases and the overlaid image. (**d**) Portion of d-spacings in different crystal planes in as-synthesized HEA and various oxide compounds. Dash signs in oxide compounds mark the d-spacings obtained from HRTEM analysis. HEA_T stands for information

extracted from (S)TEM analysis and HEA_X are obtained from XRD results. For oxide compounds, only d-spacings larger than 0.195 nm are shown to avoid overlapping of data points. (**e**) ABF image of a HEA NP after *ex situ* oxidation showing plenty of voids less than 10 nm in length. (**f**) Atomic resolution HAADF and ABF image of a HEA NP edge after oxidation. Exemplar voids are marked by red arrows. The oxide layer is highlighted. Inset in ABF image is the corresponding FFT showing the NP in <110> zone axis. (**g**) Atomic resolution HAADF and ABF image of a HEA NP in <110> zone axis. Exemplar voids are marked by red arrows and oxide layer is highlighted. A twining can be observed in both images marked with dash lines, as well as in the FFT (inset in HAABF image) with two pairs of (002) diffraction spots.

To further understand the compositional evolution in real time, *in situ* STEM-EDS are performed and shown in Movie S3. The HEA NP in the upper left corner is zoomed in and shown in Figure 5. The ABF and HAADF images are displayed together with EDS maps for Fe, Co, Ni, Cu and O at different times. Outlines of HEA and the oxide layer are also shown in the last column. At room temperature (RT), the HEA NPs show homogeneous mixing of all five elements with 2-3 nm native oxide covering the surface. The oxide contains Fe, Co, Ni and Cu and is expected to originate from initial stage of oxidation driven by the Mott electric field in the oxide layer, as predicted by the Cabrera-Mott model.[61] At 400 °C, the oxide layer begins to grow and after 2 min it is denser on left side where two adjacent NPs are present. The gradual outward diffusion of Fe, Co, Ni and Cu evidenced through EDS maps again confirms that the oxidation is guided by Kirkendall effect. This outward diffusion of transition metals and vacancies results in voids formation close to HEA surface. Then voids coalesce leading to the shrinkage of HEA NP and notable segregation of Fe, Co, Ni, Cu to the outer oxide. In addition, the *in situ* STEM-EDS analyses

suggest that the outward diffusion of transition metals occurs almost simultaneously from the beginning at 400 °C due to atomic homogeneity of as-synthesized HEA. Thus, the composition gradient in the formed oxide are mainly induced by different diffusion rates among transition metals. Figure S6 shows the Arrhenius plots of diffusion coefficients for Fe, Co, Ni and Cu in their oxides and Table S1 listed the values at 400 °C in relationship with atomic radius. Fe has the highest diffusibility at 400 °C followed by Cu, Co and Ni, which is in partial agreement with experimental observations that outward diffusion of Fe and Cu are more notable than Co and Ni. However, the diffusion coefficient does not follow the decreasing trend of atomic radius from Fe to Cu (Fe>Co>Ni>Cu) and cannot explain why Cu shows the farthest diffusion distance from HEA surface among all transition metals, while a possible explanation may be due to the highest vapor pressure of Cu among all investigated metals.[15] Future investigations of metal diffusibility and activation energy for each element in other possible oxide matrices with more than one metal element are necessary to obtain a systematic understanding.

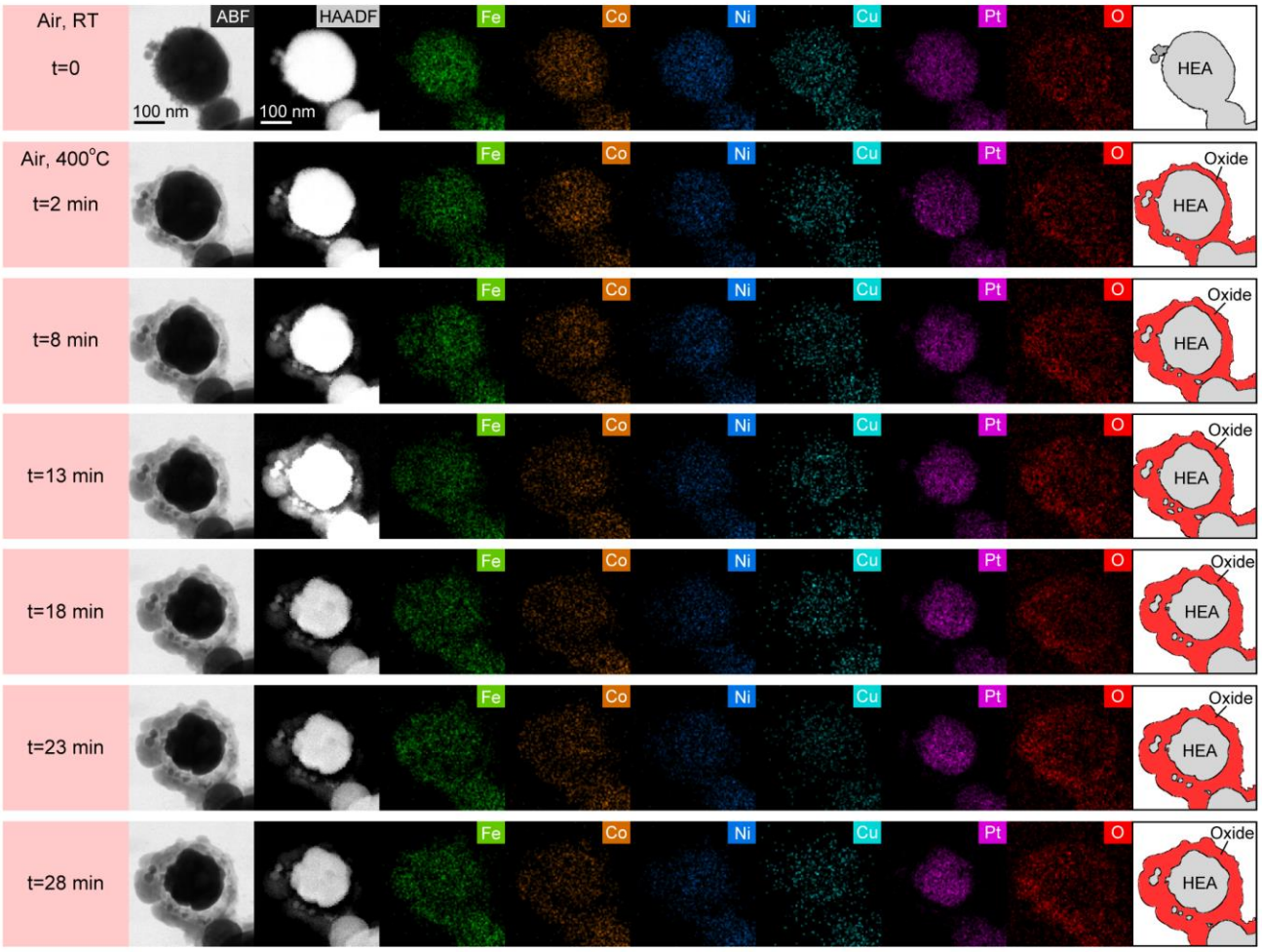

Figure 5. *In situ* EDS analysis on HEA NPs annealing in air at 400 °C. First column: time stamps; Second column: ABF images of HEA NPs annealing in air. From third column: HAADF images of the HEA NPs and corresponding EDS maps of Fe, Co, Ni, Cu, Pt and O. Last column: outlines of HEA NP and the oxide layer extracted from ABF images. The first row (t=0) corresponding to the condition at RT and is right before temperature ramping up to 400 °C.

To confirm that the phase segregation is only induced by air, *in situ* annealing of HEA NPs in vacuum environment are discussed in Supporting Note S3 and Figure S7. In addition, the electron dose rate during the *in situ* oxidation is approximately 40 $e^-/Å^2/s$ which is two orders of magnitude lower than threshold

dose rate for electron damage on oxides,[62] and also lower than other electron beam induced oxidation studies.[54, 63] The results further suggest the observed phase segregation is induced by oxidizing environments instead of electron beam effect.

Next, density functional theory (DFT) calculations were carried out to further understand the oxidation process of the HEA NPs. First, the stability of a bulk random alloy consistent with the $Fe_{0.28}Co_{0.21}Ni_{0.20}Cu_{0.08}Pt_{0.23}$ chemical composition that is inferred experimentally was investigated. The energies of several random models of the alloy assuming a HEA phase with FCC or body-centered cubic (BCC) lattice symmetry were compared. After a full structural optimization, it is found that the FCC system is 0.05 eV/atom lower in energy than the BCC one. Thus, the alloy has an FCC symmetry that agrees with the experimental results. In addition, the optimum lattice constant of the FCC lattice is found to be 3.61 Å that correlates to a d-spacing of 2.1 Å for {111} planes, which is very close to the experimentally determined d-spacing of 2.2 Å for the same planes.

The aforementioned DFT simulations employed few structural models for the alloy and thus cannot describe the configurational entropy that is key for the stability of HEAs. To address this shortcoming, calculations using a hybrid MC/MD approach based on energies and forces computed with DFT were carried out. This scheme employs short *ab initio* MD runs and random exchange between atoms at different locations, in which the last configuration is accepted or rejected using a standard Metropolis algorithm.[64,65] There are several advantages for the employed MC/MD approach as it automatically accounts for temperature, mixing entropy, atomic vibrations, while describing all interactions in the systems within first-principles methods. Following the MC/MD simulations, it is found that in equilibrium the alloy has a uniform distribution of the elements. Also, consistent with the static full optimization

calculations, the HEA with FCC symmetry is found to be ~0.05 eV/atom lower in energy than that of the BCC one at all investigated temperatures 100 - 900 °C (Figure S8).

Further, the impact of oxidation on the stability of the HEAs was studied. First, the stabilization energies due to potential segregation under oxidizing conditions were examined. Five alloy models that differ in the identity of the element enriching the top layer but is random otherwise were constructed in addition to three different alloy models with a complete random distribution. In these studies, surface slab models well representing the large ~ 50 - 200 nm NPs that are seen experimentally were employed. Further, a smaller ~1 nm NP (Figure S9-S11) was verified to display similar energy preferences. The oxidizing conditions are modeled by adsorbing oxygen on the top surface.[66-69] Starting from the initial configuration constructed using FCC with lattice constant 3.61 Å, the atomic positions were relaxed to ground state equilibrium structure at T = 0 Kelvin, and then a 4 pico-second (ps) *ab initio* MD trajectory within NVT ensemble (constant number of particles, volume and temperature) at T = 400 °C was conducted. Figure 7a shows the energies of the different models averaged over the last 2 ps measured with respect to the random alloy model. As seen, Fe, Co and Pt segregated surfaces have high energies due to their large surface energies compared to that of Ni and Cu.[70] It is noted that the high entropy of mixing is not included in the energies of Figure 7a. Hence segregated models that have lower energies than the random alloy one such as the Cu rich surface are not indicative that segregation is preferable for the pristine surface. For instance, based on ideal mixing of the elements, the configuration entropy $-k_B \sum_{i=0}^{5} x_i \ln x_i$ (k_B is Boltzmann constant and x_i is metals concentration) lowers the free energies by ~ 0.09 eV/atom for the alloy at 400°C. As will be shown later, there is no elements segregation for the pristine HEA surfaces when configurational entropy is accounted for by employing the hybrid MC/MD approach.

As seen from the energies in Figure 6a, oxidation significantly stabilizes surfaces that are rich in Fe and Co compared to the random alloy, and to a lesser extent surfaces rich in Ni and Cu. However, Pt-rich surfaces have significantly higher energy compared to the random alloy surface. Thus, under oxidation, surfaces of the NPs are expected to be poor in the noble metal Pt but rich in Fe, Co and to a lesser extent Cu and Ni. The obtained energy trends for the oxidized slab models can be rationalized by examining the formation energies of the corresponding bulk oxides. For the metal oxides, the order of the formation energies is Fe (1.7), Co (1.3), Cu (1.0), Ni (0.9), and Pt (0.6) with the numbers in parenthesis showing the DFT formation energies in eV/atom. Thus, Fe forms the most stable oxide with a formation energy of 1.7 eV/atom and Pt is the least stable one with 0.6 eV/atom. Similar conclusions can also be reached by inspecting the Ellingham diagrams of these oxides.

MC/MD simulations are then carried for the slab models to determine their equilibrium composition while accounting for temperature and entropy effects. Figure 6b shows a layer-by-layer surface decomposition obtained by analyzing equilibrium configurations from the MC/MD simulations. An exemplary configuration is shown in Figure 6c. As seen from the figure, there is a strong segregation preference for some elements to the top layers under oxidation conditions. For instance, compared to the bare surface, there is a notable enrichment of Fe and Co in the top exposed layers but a significant reduction of Pt. This is also consistent with the trends inferred from the energies of the segregated models of Figure 6a. Further, the oxidation process increases the thickness of the substrate resulting in the formation of an additional layer. As seen in Figure 6c, an equilibrium configuration during the oxidation shows formation of vacancies in subsurface layers due to a Kirkendall effect from the inequivalent inner/outer diffusion of oxygen/metal. Also, the oxidized slab models retain FCC symmetry away from

the surface, again consistent with the experimentally observed FCC lattices after oxidation. Although the slab models are relatively small to show the formation of any nanocrystalline oxides, Bader charge analysis in Table S2 suggests that the chemical environment of the metals in the oxide layer are similar to the corresponding Fe_2O_3, CoO, NiO and CuO oxides that are inferred experimentally.

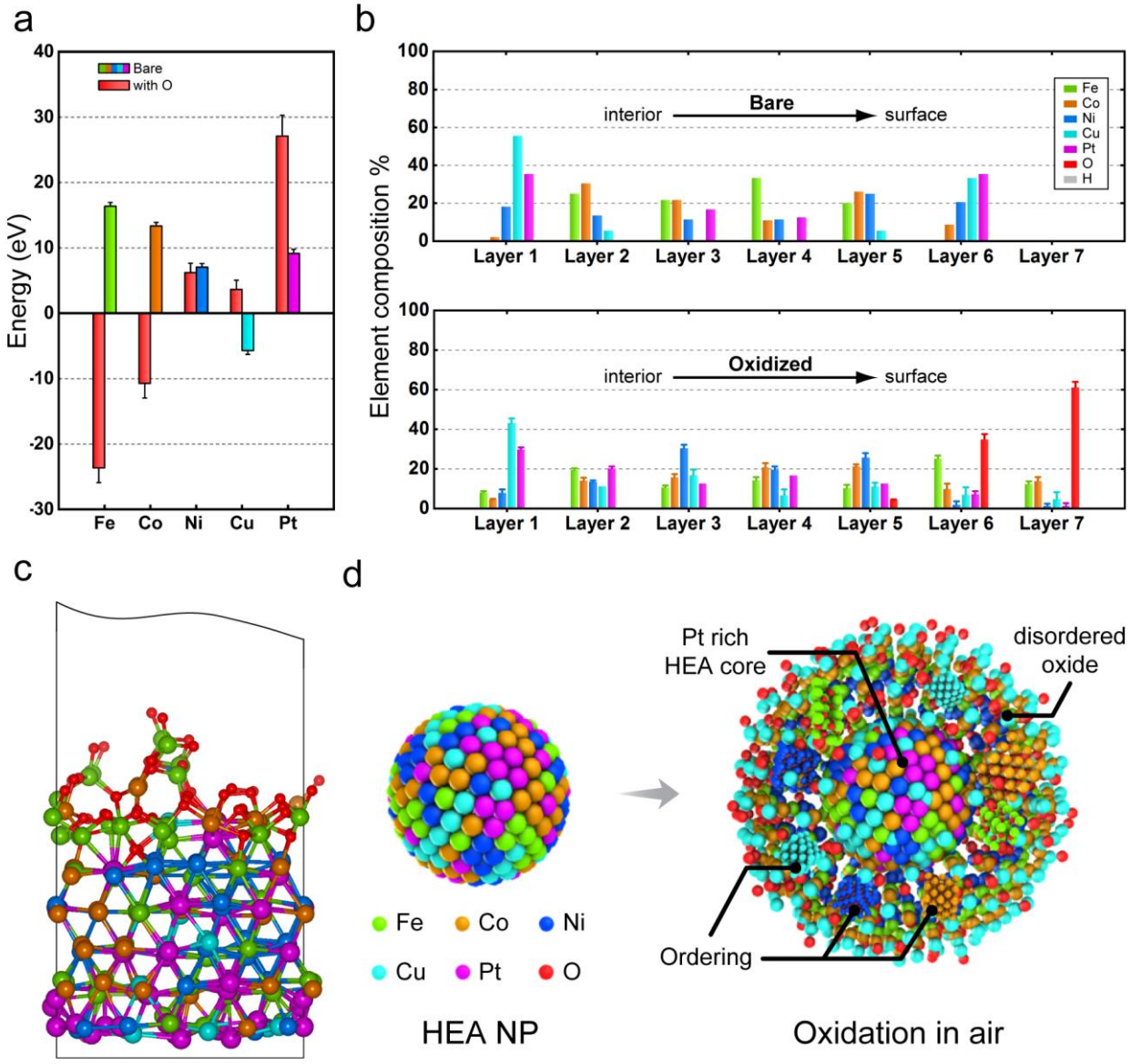

Figure 6. (**a**) Total energies for slab models with different elements segregation compared to the random alloy model. For each model, the corresponding energy of the oxidized are shown as red. Negative values

indicate enhanced stability compared to random alloy without accounting for configurational entropy. Statistical errors for the energies extracted from molecular trajectory are shown. (**b**) Equilibrium layer-by-layer surface composition for bare and oxidized surfaces at 400 °C. The error bars indicate statistical errors from equilibrium structures obtained from MC/MD. Oxidation increases the thickness of the slab and leads to the formation of an extra layer. (**c**) Exemplary atomic model for an oxidized slab from the MC/MD ensemble after equilibration. (**d**) Schematic illustration of the oxidation process of HEA NPs.

The schematic shown in Figure 6d illustrates the oxidation process of HEA NPs. The HEA NPs are initially homogeneously mixed in atomic level at RT, while at 400 °C in air the outward diffusion of transition metals resulted in oxide layer enriched with Fe, Co, Ni and Cu. Kirkendall effects guided the process and leads to a concentration gradient in the oxide. Localized ordered lattices from transition metal oxides can be seen to form in the overall disordered oxide region. The HEA core retains FCC structure but shrinks in size due to deficiency of transition metals. Non-reactive Pt stays in the HEA core region at all time during the oxidation process. The formed disordered oxide serves as diffusion barrier to prevent further oxidation of the HEA core, resulting in a logarithmic rate constant for oxidation kinetic that differs from the conventional high-temperature oxidation theory.

Conclusion

The present work reports *in situ* TEM observation and DFT study of phase segregation in HEA NPs during high-temperature oxidation process. The oxidation of HEA NPs is governed by Kirkendall effects with

logarithmic rate constants that differs from high-temperature oxidation theory with parabolic prediction and is much slower than monometallic and bimetallic NPs. HRTEM and analytical EDS/EELS provide direct evidence of transition metals segregation by outward diffusion and disordered oxide layer formation. The possible sluggish diffusion in HEA and formation of disordered oxide can slow down the oxidation kinetics compared to conventional monometallic and bimetallic systems. In addition, localized ordering is identified in the oxide layer that can originate from Fe_2O_3, CoO, NiO and CuO crystallites. Simulations using hybrid MC/MD simulations based on DFT energies and forces confirm the stabilization of the alloy solution for the bare and oxidized surfaces, and show that the oxidation drive Fe, Co, Ni and Cu segregation to the top layers in agreement with experimental results. The present study is crucial for understanding HEA behavior in oxidizing environments, and provides insights in designing high temperature resistant materials, durable catalysts, and corrosion resistance alloys for various applications.

Methods

HEA NPs synthesis. HEA NPs containing Fe, Co, Ni, Cu, and Pt were synthesized based on the method in previous study[15] and stored in glove box under Ar. The as-synthesized sample were dispersed in ethanol and sonicated for 2 min in a bath sonicator (Branson 3800, 40kHz, 110W) before (S)TEM experiments.

***In situ* TEM experiment in vacuum.** A furnace based heating holder (Gatan, Inc.) is used for heating experiments in vacuum condition. HEA sample dispersion is drop-casted onto Mo grid and then inserted into a spherical aberration corrected JEOL JEM-ARM 200CF with cold field emission source operating

at 200 kV. Temperature was ramped up from RT to 400 °C with a 100 °C interval every 1 hr, and ramped down to RT after another 1 hr staying at 400 °C.

***In situ* gas flow TEM experiment.** A Hummingbird Scientific gas-cell TEM holder was used (Figure 2a). 1 μL HEA sample dispersion was drop-casted on microchip equipped with heater and dried under air, then paired with another microchip to assemble the holder. The microchips have an electron transparent silicon nitride (Si_3N_4) viewing window with 50 nm in thickness. The distance between top and bottom microchip was controlled by a 250 nm spacer. All gases are flowed under constant volumetric flow rate of 0.5 sccm with pressure inside the cell to be approximately 1 atmosphere. After loading the holder and flowing 100% pure nitrogen (N_2) gas at RT for 30 min, the gas was changed to dry laboratory grade air (containing ~21 vol. % O_2) and temperature was ramped up to 400 °C within 2 min and kept constant afterwards. When finished the temperature was ramped down back to RT within 1 min. Unless otherwise specified, the electron beam was kept blocked at all time except initial TEM alignment, focusing and image acquisition to minimize electron beam effects. All *in situ* TEM experiments were carried out using a field emission JEOL 2100F microscope operated at 200kV.

***In situ* gas flow STEM experiment.** The *in situ* STEM and EDS experiments were performed using spherical aberration corrected JEOL JEM-ARM 200CF with a cold field emission source operating at 200 kV combined with a gas-cell TEM holder from Protochips, Inc. The spacer distance between two microchips was 5 μm. The holder was assembled after drop-casted HEA samples onto one of the microchips. Gas channels were opened to allow sample expose in air environment for oxidation process. The local temperature was monitored in real-time and kept constant at 400 °C. *In situ* EDS maps were

acquired with JEOL dual silicon drift detectors. The area of a single detector is 100 mm^2 and the solid angle for this dual EDS system is 1.8 sr. EDS maps were collected at RT and every 5 min at 400 °C.

***Ex situ* annealing experiment in air.** *Ex situ* oxidation were performed in two different methods. In the first method, HEA NPs were firstly drop-casted onto Mo grid. The grid was placed onto a hot plate in air atmosphere with temperature preset to 400 °C for 1 hr. Then the grid is cool down in air before (S)TEM characterization. In the second method, the gas-cell TEM holder was assembled with HEA NPs but was not inserted into the microscope. The holder was then flowed with air and temperature ramped up in same way as *in situ* TEM experiment. After finished and cool down to RT, the HEA NPs on microchip is characterized directly by (S)TEM.

Electron microscopy characterization. *Post situ* sample on microchips were characterized using a self-designed (S)TEM specimen holder (patent pending). STEM images were acquired by a spherical aberration corrected JEOL JEM-ARM 200CF with a cold field emission source operating at 200 kV, at 22 mrad convergence semi-angle. *Post situ* EDS maps were acquired with Oxford X-Max 100TLE windowless silicon drift detector. EELS were acquired using a Gatan GIF Quantum spectrometer with an entrance aperture of 5 mm in dual-EELS mode. EELS maps were extracted from transition metals $L_{2,3}$-edges, O *K*-edge using power law fitting background subtraction after energy drift correction and Fourier-ratio deconvolution. Transition metal L_3/L_2 white-line intensity ratio was determined by applying Hartree-Slater cross section step-functions following the previous reported method.[56]

Density functional theory calculations. First-principles DFT calculations are employed using the Perdew-Burke-Ernzerhof[71] exchange-correlational functional to solve the Kohn-Sham equations. The electronic self-consistent loops are terminated with energy-change tolerance of 1×10^{-8} eV. Bulk

calculations for the alloy or for the elementary metals, or their oxides and hydrides are carried out using the Vienna *ab initio* simulation package (VASP)[72-74] with a planewave cutoff of 400 eV. For these calculations, we used a dense gamma-centered k-grid with a 0.24 $Å^{-1}$ spacing between k-points. This is equivalent to 8 x 8 x 8 mesh for bulk metals with conventional four atom FCC unit cell. The electron-nucleus interactions are described using the projector augmented wave (PAW) method as implemented in VASP.[75] The hybrid MC/MD simulations are carried out using VASP computed energies and forces. For these calculations, we employed softer PAW potentials, a 300 eV planewave cutoff, and gamma point sampling of the Brillouin zone. It is found that equilibrium is reached by conducting a total of 1000 steps where each hybrid step corresponds to a potential MC swap between two random metal atoms followed by 40 molecular dynamics steps with a 1 femtosecond timestep.[65] The *ab initio* molecular dynamics simulations for the slab models or the isolated NPs are carried out using CP2K using DZVP-MOLOPT-SR-GTH basis sets and GTH norm-conserving potentials.[76,77] All of the calculations are done within the spin-averaged approximation. For bulk FCC random alloy model, spin-polarized calculations yield a lattice constant 3.67Å that is close to the value of 3.61Å obtained from spin-unpolarized calculations.

Acknowledgments

R. Shahbazian-Yassar acknowledges financial support from the National Science Foundation (Award No. DMR-1809439). W. Saidi acknowledges financial support from the National Science Foundation (Award No. DMR-1809085). The computational work is supported in part by the University of Pittsburgh Center for Research Computing through the resources provided, and Argonne Leadership Computing Facility, which is a DOE Office of Science User Facility supported under Contract DE-AC02-06CH11357. This

work was performed, in part, at the Center for Nanoscale Materials, a U.S. Department of Energy Office of Science User Facility, and supported by the U.S. Department of Energy, Office of Science, under Contract No. DE-AC02-06CH11357. This work made use of the JEOL JEM-ARM 200CF and JEOL JEM-3010 in the Electron Microscopy Service (Research Resources Center, UIC). The acquisition of the UIC JEOL JEM-ARM 200CF was supported by a MRI-R2 grant from the National Science Foundation (DMR-0959470). We thank Dr. Fengyuan Shi from UIC for the assistance on (S)TEM experiments. Partial of this work made use of the EPIC facility of Northwestern University's *NUANCE* Center, which has received support from the Soft and Hybrid Nanotechnology Experimental (SHyNE) Resource (NSF ECCS-1542205); the MRSEC program (NSF DMR-1720139) at the Materials Research Center; the International Institute for Nanotechnology (IIN); the Keck Foundation; and the State of Illinois, through the IIN. M. Zachariah acknowledges support from an ONR MURI.

Author Contribution

B. Song and R. Shahbazian-Yassar conceived the idea. Y. Yang, P. Ghildiyal, and M. Zachariah prepared the HEA samples. B. Song carried out the (S)TEM and *in situ* TEM experiments. M. Rabbani, T. Yang, and W. Saidi carried out the DFT calculations. Y. Liu, K. He, X. Hu, Y. Yuan, and V. Dravid provided necessary (S)TEM support. B. Song wrote the paper under the direction of R. Shahbazian-Yassar. All authors contributed to the discussion and writing of the manuscript.

Supporting Information

The Supporting Information is available free of charge at http://pubs.acs.org.

In situ TEM video of HEA NPs oxidation in air at 400 °C 64 times faster (Movie S1); *In situ* TEM video showing Co NPs oxidation in air at 400 °C 4 times faster (Movie S2); *In situ* STEM-EDS maps of HEA NPs oxidation in air at 400 °C (Movie S3); As-synthesized HEA NPs composition (Figure S1); Comparison between HEA NPs and monometallic Co NPs oxidation kinetics (Figure S2); *Post situ* STEM-EDS results of HEA NPs in Figure 3a (Figure S3); STEM-EDS on HEA NPs without electron beam exposure (Supporting Note S1 and Figure S4); Structural characterization of HEA NPs before and after *ex situ* oxidation (Supporting Note S2 and Figure S5); Arrhenius plots of diffusion coefficient with temperature (Figure S6); Diffusion coefficient from Figure S6 and atomic radius (Table S1); *In situ* annealing of HEA NPs in vacuum (Supporting Note S3 and Figure S7); Comparison between FCC and BCC energies of HEA from simulations (Figure S8); Models for HEA NPs before (Figure S9) and after oxidation (Figure S10); Normalized energies for the models in Figure S9 and S10 in comparison with random alloy model (Figure S11); Bader charge analysis for several metals and oxides (Table S2).

References

(1) Tsai, M.-H.; Yeh, J.-W. High-Entropy Alloys: A Critical Review. *Materials Research Letters* **2014**, *2*, 107-123.

(2) Ye, Y. F.; Wang, Q.; Lu, J.; Liu, C. T.; Yang, Y. High-Entropy Alloy: Challenges and Prospects. *Mater. Today* **2016**, *19*, 349-362.

(3) Chen, J.; Zhou, X.; Wang, W.; Liu, B.; Lv, Y.; Yang, W.; Xu, D.; Liu, Y. A Review on Fundamental of High Entropy Alloys with Promising High–Temperature Properties. *J. Alloys Compd.* **2018**, *760*, 15-30.

(4) George, E. P.; Raabe, D.; Ritchie, R. O. High-Entropy Alloys. *Nature Reviews Materials* **2019**, *4*, 515-534.

(5) Yeh, J. W.; Chen, S. K.; Lin, S. J.; Gan, J. Y.; Chin, T. S.; Shun, T. T.; Tsau, C. H.; Chang, S. Y. Nanostructured High-Entropy Alloys with Multiple Principal Elements: Novel Alloy Design Concepts and Outcomes. *Adv. Eng. Mater.* **2004**, *6*, 299-303.

(6) Otto, F.; Yang, Y.; Bei, H.; George, E. P. Relative Effects of Enthalpy and Entropy on the Phase Stability of Equiatomic High-Entropy Alloys. *Acta Mater.* **2013**, *61*, 2628-2638.

(7) Fu, Z.; Chen, W.; Wen, H.; Zhang, D.; Chen, Z.; Zheng, B.; Zhou, Y.; Lavernia, E. J. Microstructure and Strengthening Mechanisms in an Fcc Structured Single-Phase Nanocrystalline $Co_{25}Ni_{25}Fe_{25}Al_{7.5}Cu_{17.5}$ High-Entropy Alloy. *Acta Mater.* **2016**, *107*, 59-71.

(8) Sriharitha, R.; Murty, B. S.; Kottada, R. S. Alloying, Thermal Stability and Strengthening in Spark Plasma Sintered Alxcocrcufeni High Entropy Alloys. *J. Alloys Compd.* **2014**, *583*, 419-426.

(9) Fang, S.; Chen, W.; Fu, Z. Microstructure and Mechanical Properties of Twinned $Al_{0.5}CrFeNiCo_{0.3}C_{0.2}$ High Entropy Alloy Processed by Mechanical Alloying and Spark Plasma Sintering. *Materials & Design (1980-2015)* **2014**, *54*, 973-979.

(10) Zou, Y.; Wheeler, J. M.; Ma, H.; Okle, P.; Spolenak, R. Nanocrystalline High-Entropy Alloys: A New Paradigm in High-Temperature Strength and Stability. *Nano Lett.* **2017**, *17*, 1569-1574.

(11) Brif, Y.; Thomas, M.; Todd, I. The Use of High-Entropy Alloys in Additive Manufacturing. *Scripta Mater.* **2015**, *99*, 93-96.

(12) Fujieda, T.; Shiratori, H.; Kuwabara, K.; Kato, T.; Yamanaka, K.; Koizumi, Y.; Chiba, A. First Demonstration of Promising Selective Electron Beam Melting Method for Utilizing High-Entropy Alloys

as Engineering Materials. *Mater. Lett.* **2015**, *159*, 12-15.

(13) Gorsse, S.; Hutchinson, C.; Gouné, M.; Banerjee, R. Additive Manufacturing of Metals: A Brief Review of the Characteristic Microstructures and Properties of Steels, Ti-6Al-4V and High-Entropy Alloys. *Science and Technology of Advanced Materials* **2017**, *18*, 584-610.

(14) Yao, Y.; Huang, Z.; Xie, P.; Lacey, S. D.; Jacob, R. J.; Xie, H.; Chen, F.; Nie, A.; Pu, T.; Rehwoldt, M.; Yu, D.; Zachariah, M. R.; Wang, C.; Shahbazian-Yassar, R.; Li, J.; Hu, L. Carbothermal Shock Synthesis of High-Entropy-Alloy Nanoparticles. *Science* **2018**, *359*, 1489-1494.

(15) Yang, Y.; Song, B.; Ke, X.; Xu, F.; Bozhilov, K. N.; Hu, L.; Shahbazian-Yassar, R.; Zachariah, M. R. Aerosol Synthesis of High Entropy Alloy Nanoparticles. *Langmuir* **2020**, *36*, 1985-1992.

(16) Shi, Y.; Yang, B.; Liaw, P. Corrosion-Resistant High-Entropy Alloys: A Review. *Metals* **2017**, *7*, 43.

(17) Daoud, H. M.; Manzoni, A. M.; Völkl, R.; Wanderka, N.; Glatzel, U. Oxidation Behavior of $Al_8Co_{17}Cr_{17}Cu_8Fe_{17}Ni_{33}$, $Al_{23}Co_{15}Cr_{23}Cu_8Fe_{15}Ni_{15}$, and $Al_{17}Co_{17}Cr_{17}Cu_{17}Fe_{17}Ni_{17}$ Compositionally Complex Alloys (High-Entropy Alloys) at Elevated Temperatures in Air. *Adv. Eng. Mater.* **2015**, *17*, 1134-1141.

(18) Kai, W.; Li, C. C.; Cheng, F. P.; Chu, K. P.; Huang, R. T.; Tsay, L. W.; Kai, J. J. Air-Oxidation of Feconicr-Based Quinary High-Entropy Alloys at 700–900 °C. *Corros. Sci.* **2017**, *121*, 116-125.

(19) Butler, T. M.; Weaver, M. L. Oxidation Behavior of Arc Melted Alcocrfeni Multi-Component High-Entropy Alloys. *J. Alloys Compd.* **2016**, *674*, 229-244.

(20) Laplanche, G.; Volkert, U. F.; Eggeler, G.; George, E. P. Oxidation Behavior of the Crmnfeconi High-Entropy Alloy. *Oxid. Met.* **2016**, *85*, 629-645.

(21) Gorr, B.; Azim, M.; Christ, H. J.; Mueller, T.; Schliephake, D.; Heilmaier, M. Phase Equilibria,

Microstructure, and High Temperature Oxidation Resistance of Novel Refractory High-Entropy Alloys. *J. Alloys Compd.* **2015**, *624*, 270-278.

(22) Kai, W.; Li, C. C.; Cheng, F. P.; Chu, K. P.; Huang, R. T.; Tsay, L. W.; Kai, J. J. The Oxidation Behavior of an Equimolar Feconicrmn High-Entropy Alloy at 950°C in Various Oxygen-Containing Atmospheres. *Corros. Sci.* **2016**, *108*, 209-214.

(23) Xia, W.; Yang, Y.; Meng, Q.; Deng, Z.; Gong, M.; Wang, J.; Wang, D.; Zhu, Y.; Sun, L.; Xu, F.; Li, J.; Xin, H. L. Bimetallic Nanoparticle Oxidation in Three Dimensions by Chemically Sensitive Electron Tomography and *in Situ* Transmission Electron Microscopy. *ACS Nano* **2018**, *12*, 7866-7874.

(24) Zhu, Y.; Sushko, P. V.; Melzer, D.; Jensen, E.; Kovarik, L.; Ophus, C.; Sanchez-Sanchez, M.; Lercher, J. A.; Browning, N. D. Formation of Oxygen Radical Sites on Movnbteox by Cooperative Electron Redistribution. *J. Am. Chem. Soc.* **2017**, *139*, 12342-12345.

(25) Zou, L.; Li, J.; Zakharov, D.; Stach, E. A.; Zhou, G. *In Situ* Atomic-Scale Imaging of the Metal/Oxide Interfacial Transformation. *Nat Commun* **2017**, *8*, 307.

(26) Wang, C.-M.; Genc, A.; Cheng, H.; Pullan, L.; Baer, D. R.; Bruemmer, S. M. *In-Situ* TEM Visualization of Vacancy Injection and Chemical Partition During Oxidation of Ni-Cr Nanoparticles. *Sci. Rep.* **2014**, *4*, 3683.

(27) Jeangros, Q.; Hansen, T. W.; Wagner, J. B.; Damsgaard, C. D.; Dunin-Borkowski, R. E.; Hébert, C.; Van herle, J.; Hessler-Wyser, A. Reduction of Nickel Oxide Particles by Hydrogen Studied in an Environmental TEM. *J. Mater. Sci.* **2013**, *48*, 2893-2907.

(28) Prestat, E.; Kulzick, M. A.; Dietrich, P. J.; Smith, M. M.; Tien, M. E. P.; Burke, M. G.; Haigh, S. J.; Zaluzec, N. J. *In Situ* Industrial Bimetallic Catalyst Characterization Using Scanning Transmission

Electron Microscopy and X‐Ray Absorption Spectroscopy at One Atmosphere and Elevated Temperature. *ChemPhysChem* **2017**, *18*, 2151-2156.

(29) Xin, H. L.; Niu, K.; Alsem, D. H.; Zheng, H. *In Situ* TEM Study of Catalytic Nanoparticle Reactions in Atmospheric Pressure Gas Environment. *Microsc. Microanal.* **2013**, *19*, 1558-1568.

(30) Jiang, Y.; Li, H.; Wu, Z.; Ye, W.; Zhang, H.; Wang, Y.; Sun, C.; Zhang, Z. *In Situ* Observation of Hydrogen-Induced Surface Faceting for Palladium–Copper Nanocrystals at Atmospheric Pressure. *Angew. Chem. Int. Ed.* **2016**, *55*, 12427-12430.

(31) Dembélé, K.; Bahri, M.; Melinte, G.; Hirlimann, C.; Berliet, A.; Maury, S.; Gay, A. S.; Ersen, O. Insight by *in Situ* Gas Electron Microscopy on the Thermal Behaviour and Surface Reactivity of Cobalt Nanoparticles. *ChemCatChem* **2018**, *10*, 4004-4009.

(32) Tan, S. F.; Chee, S. W.; Baraissov, Z.; Jin, H.; Tan, T. L.; Mirsaidov, U. Real‐Time Imaging of Nanoscale Redox Reactions over Bimetallic Nanoparticles. *Adv. Funct. Mater.* **2019**, *29*, 1903242.

(33) Altantzis, T.; Lobato, I.; De Backer, A.; Béché, A.; Zhang, Y.; Basak, S.; Porcu, M.; Xu, Q.; Sánchez-Iglesias, A.; Liz-Marzán, L. M.; Van Tendeloo, G.; Van Aert, S.; Bals, S. Three-Dimensional Quantification of the Facet Evolution of Pt Nanoparticles in a Variable Gaseous Environment. *Nano Lett.* **2019**, *19*, 477-481.

(34) Song, B.; Yang, T. T.; Yuan, Y.; Sharifi-Asl, S.; Cheng, M.; Saidi, W. A.; Liu, Y.; Shahbazian-Yassar, R. Revealing Sintering Kinetics of MoS_2-Supported Metal Nanocatalysts in Atmospheric Gas Environments *via* Operando Transmission Electron Microscopy. *ACS Nano* **2020**, *14*, 4074-4086.

(35) Li, Y.; Zakharov, D.; Zhao, S.; Tappero, R.; Jung, U.; Elsen, A.; Baumann, P.; Nuzzo, R. G.; Stach, E. A.; Frenkel, A. I. Complex Structural Dynamics of Nanocatalysts Revealed in Operando Conditions by

Correlated Imaging and Spectroscopy Probes. *Nat. Commun.* **2015**, *6*, 7583.

(36) Wu, Y. A.; Li, L.; Li, Z.; Kinaci, A.; Chan, M. K.; Sun, Y.; Guest, J. R.; McNulty, I.; Rajh, T.; Liu, Y. Visualizing Redox Dynamics of a Single Ag/AgCl Heterogeneous Nanocatalyst at Atomic Resolution. *ACS Nano* **2016**, *10*, 3738-3746.

(37) Han, L.; Meng, Q.; Wang, D.; Zhu, Y.; Wang, J.; Du, X.; Stach, E. A.; Xin, H. L. Interrogation of Bimetallic Particle Oxidation in Three Dimensions at the Nanoscale. *Nat Commun* **2016**, *7*, 13335.

(38) Wagner, C. Beitrag Zur Theorie Des Anlaufvorgangs. *Z. Phys. Chem.* **1933**, *21*, 25-41.

(39) Zhdanov, V. P.; Kasemo, B. Cabrera–Mott Kinetics of Oxidation of nm-Sized Metal Particles. *Chem. Phys. Lett.* **2008**, *452*, 285-288.

(40) Miley, H. A. Theory of Oxidation and Tarnishing of Metals. *Transactions of The Electrochemical Society* **1942**, *81*, 391.

(41) Henz, B. J.; Hawa, T.; Zachariah, M. R. On the Role of Built-in Electric Fields on the Ignition of Oxide Coated Nanoaluminum: Ion Mobility *versus* Fickian Diffusion. *J. Appl. Phys.* **2010**, *107*, 024901.

(42) Anderson, B. D.; Tracy, J. B. Nanoparticle Conversion Chemistry: Kirkendall Effect, Galvanic Exchange, and Anion Exchange. *Nanoscale* **2014**, *6*, 12195-12216.

(43) Grammatikopoulos, P.; Sowwan, M.; Kioseoglou, J. Computational Modeling of Nanoparticle Coalescence. *Advanced Theory and Simulations* **2019**, *2*, 1900013.

(44) Rai, A.; Park, K.; Zhou, L.; Zachariah, M. R. Understanding the Mechanism of Aluminium Nanoparticle Oxidation. *Combustion Theory and Modelling* **2006**, *10*, 843-859.

(45) Chen, Y.; Zhao, X.; Xiao, P. Effect of Surface Curvature on Oxidation of a Mcraly Coating. *Corros. Sci.* **2020**, *163*, 108256.

(46) Laplanche, G.; Kostka, A.; Reinhart, C.; Hunfeld, J.; Eggeler, G.; George, E. P. Reasons for the Superior Mechanical Properties of Medium-Entropy Crconi Compared to High-Entropy Crmnfeconi. *Acta Mater.* **2017**, *128*, 292-303.

(47) Chen, S.; Oh, H. S.; Gludovatz, B.; Kim, S. J.; Park, E. S.; Zhang, Z.; Ritchie, R. O.; Yu, Q. Real-Time Observations of Trip-Induced Ultrahigh Strain Hardening in a Dual-Phase Crmnfeconi High-Entropy Alloy. *Nat. Commun.* **2020**, *11*, 826.

(48) Ahn, C. C.; Krivanek, O. L. *EELS Atlas: A Reference Guide of Electron Energy Loss Spectra Covering All Stable Elements*; ASU HREM Facility & Gatan Inc.: Warrendale, PA, USA, **1983**; 1-92.

(49) Ewels, P.; Sikora, T.; Serin, V.; Ewels, C. P.; Lajaunie, L. A Complete Overhaul of the Electron Energy-Loss Spectroscopy and X-Ray Absorption Spectroscopy Database: Eelsdb.Eu. *Microsc. Microanal.* **2016**, *22*, 717-724.

(50) Feldhoff, A.; Martynczuk, J.; Arnold, M.; Myndyk, M.; Bergmann, I.; Šepelák, V.; Gruner, W.; Vogt, U.; Hähnel, A.; Woltersdorf, J. Spin-State Transition of Iron in $(Ba_{0.5}Sr_{0.5})(Fe_{0.8}Zn_{0.2})O_3$-Δ Perovskite. *J. Solid State Chem.* **2009**, *182*, 2961-2971.

(51) Zhao, Y.; Feltes, T. E.; Regalbuto, J. R.; Meyer, R. J.; Klie, R. F. *In Situ* Electron Energy Loss Spectroscopy Study of Metallic Co and Co Oxides. *J. Appl. Phys.* **2010**, *108*, 063704.

(52) Potapov, P. L.; Kulkova, S. E.; Schryvers, D.; Verbeeck, J. Structural and Chemical Effects on EELS $L_{3,2}$ Ionization Edges in Ni-Based Intermetallic Compounds. *Phys. Rev. B* **2001**, *64*, 184110.

(53) Ngantcha, J. P.; Gerland, M.; Kihn, Y.; Rivière, A. Correlation between Microstructure and Mechanical Spectroscopy of a Cu-Cu_2O Alloy between 290 K and 873 K. *Eur. Phys. J. Appl. Phys.* **2005**, *29*, 83-89.

(54) Guo, J.; Haberfehlner, G.; Rosalie, J.; Li, L.; Duarte, M. J.; Kothleitner, G.; Dehm, G.; He, Y.; Pippan, R.; Zhang, Z. *In Situ* Atomic-Scale Observation of Oxidation and Decomposition Processes in Nanocrystalline Alloys. *Nat Commun* **2018**, *9*, 946.

(55) Wang, F.; Malac, M.; Egerton, R. F. Energy-Loss Near-Edge Fine Structures of Iron Nanoparticles. *Micron* **2006**, *37*, 316-323.

(56) Wang, Z. L.; Yin, J. S.; Jiang, Y. D. EELS Analysis of Cation Valence States and Oxygen Vacancies in Magnetic Oxides. *Micron* **2000**, *31*, 571-580.

(57) Wang, Z. L.; Yin, J. S.; Mo, W. D.; Zhang, Z. J. *In-Situ* Analysis of Valence Conversion in Transition Metal Oxides Using Electron Energy-Loss Spectroscopy. *The Journal of Physical Chemistry B* **1997**, *101*, 6793-6798.

(58) Varela, M.; Oxley, M. P.; Luo, W.; Tao, J.; Watanabe, M.; Lupini, A. R.; Pantelides, S. T.; Pennycook, S. J. Atomic-Resolution Imaging of Oxidation States in Manganites. *Phys. Rev. B* **2009**, *79*.

(59) Jeurgens, L. P. H.; Sloof, W. G.; Tichelaar, F. D.; Mittemeijer, E. J. Thermodynamic Stability of Amorphous Oxide Films on Metals: Application to Aluminum Oxide Films on Aluminum Substrates. *Phys. Rev. B* **2000**, *62*, 4707-4719.

(60) Fehlner, F. P. Low Temperature Oxidation, the Role of Vitreous Oxides. **1986**.

(61) Cabrera, N.; Mott, N. F. Theory of the Oxidation of Metals. *Rep. Prog. Phys.* **1949**, *12*, 163-184.

(62) Jiang, N. Electron Beam Damage in Oxides: A Review. *Rep. Prog. Phys.* **2015**, *79*, 016501.

(63) Zhang, D.; Jin, C.; Tian, H.; Xiong, Y.; Zhang, H.; Qiao, P.; Fan, J.; Zhang, Z.; Li, Z. Y.; Li, J. An *in Situ* TEM Study of the Surface Oxidation of Palladium Nanocrystals Assisted by Electron Irradiation. *Nanoscale* **2017**, *9*, 6327-6333.

(64) Purton, J. A.; Barrera, G. D.; Allan, N. L.; Blundy, J. D. Monte Carlo and Hybrid Monte Carlo/Molecular Dynamics Approaches to Order− Disorder in Alloys, Oxides, and Silicates. *The Journal of Physical Chemistry B* **1998**, *102*, 5202-5207.

(65) Widom, M.; Huhn, W. P.; Maiti, S.; Steurer, W. Hybrid Monte Carlo/Molecular Dynamics Simulation of a Refractory Metal High Entropy Alloy. *Metallurgical and Materials Transactions A* **2013**, *45*, 196-200.

(66) Zhu, Q.; Zou, L.; Zhou, G.; Saidi, W. A.; Yang, J. C. Early and Transient Stages of Cu Oxidation: Atomistic Insights from Theoretical Simulations and *in Situ* Experiments. *Surf Sci.* **2016**, *652*, 98-113.

(67) Curnan, M. T.; Andolina, C. M.; Li, M.; Zhu, Q.; Chi, H.; Saidi, W. A.; Yang, J. C. Connecting Oxide Nucleation and Growth to Oxygen Diffusion Energetics on Stepped Cu(011) Surfaces: An Experimental and Theoretical Study. *J. Phys. Chem. C* **2018**, *123*, 452-463.

(68) Saidi, W. A.; Lee, M.; Li, L.; Zhou, G.; McGaughey, A. J. H. *Ab Initio* Atomistic Thermodynamics Study of the Early Stages of Cu(100) Oxidation. *Phys. Rev. B* **2012**, *86*, 245429.

(69) Zhu, Q.; Saidi, W. A.; Yang, J. C. Step-Edge Directed Metal Oxidation. *J. Phys. Chem. Lett.* **2016**, *7*, 2530-2536.

(70) Vitos, L.; Ruban, A. V.; Skriver, H. L.; Kollár, J. The Surface Energy of Metals. *Surf Sci.* **1998**, *411*, 186-202.

(71) Perdew, J. P.; Burke, K.; Ernzerhof, M. Generalized Gradient Approximation Made Simple. *Phys. Rev. Lett.* **1996**, *77*, 3865-3868.

(72) Kresse, G.; Hafner, J. *Ab Initio* Molecular Dynamics for Liquid Metals. *Phys. Rev. B* **1993**, *47*, 558.

(73) Kresse, G.; Hafner, J. *Ab Initio* Molecular Dynamics for Open-Shell Transition Metals. *Phys. Rev.*

B **1993**, *48*, 13115.

(74) Kresse, G.; Hafner, J. *Ab Initio* Molecular-Dynamics Simulation of the Liquid-Metal-Amorphous-Semiconductor Transition in Germanium. *Phys. Rev. B* **1994**, *49*, 14251.

(75) Kresse, G.; Joubert, D. From Ultrasoft Pseudopotentials to the Projector Augmented-Wave Method. *Phys. Rev. B* **1999**, *59*, 1758-1775.

(76) Goedecker, S.; Teter, M.; Hutter, J. Separable Dual-Space Gaussian Pseudopotentials. *Phys. Rev. B* **1996**, *54*, 1703-1710.

(77) VandeVondele, J.; Krack, M.; Mohamed, F.; Parrinello, M.; Chassaing, T.; Hutter, J. Quickstep: Fast and Accurate Density Functional Calculations Using a Mixed Gaussian and Plane Waves Approach. *Comput. Phys. Commun.* **2005**, *167*, 103-128.